Multi-Way Lossless Outphasing System Based on an All-Transmission-Line Combiner

Taylor W. Barton, *Member, IEEE,* Alexander S. Jurkov, *Student Member, IEEE,*
Prathamesh H. Pednekar *Student Member, IEEE,* David J. Perreault *Fellow, IEEE*

Abstract—**A lossless power combining network comprising cascaded transmission line segments in a tree structure is introduced for a multi-way outphasing architecture. This architecture addresses the suboptimal loading conditions in Chireix outphasing transmitters while offering a compact and microwave-friendly implementation compared to previous techniques. In the proposed system, four saturated power amplifiers interact through an all-transmission-line power combining network to produce nearly ideal resistive load modulation of the branch power amplifiers over a 10:1 range of output powers. This work focuses on the operation of the combining network, deriving analytical expressions for input-port admittance characteristics and an outphasing control strategy to modulate output power while minimizing reactive loading of the saturated branch amplifiers. A methodology for combiner design is given, along with a combiner design example for compact layout. An experimental four-way outphasing amplifier system operating at 2.14 GHz demonstrates the technique with greater than 60% drain efficiency for an output power range of 6.2 dB. The system demonstrates a W-CDMA modulated signal with a 9.15-dB peak to average power ratio (PAPR) with 54.5% average modulated efficiency at 41.1 dBm average output power.**

Index Terms—**base stations, outphasing, power amplifier (PA), wideband code division multiple access (W-CDMA), Chireix, LINC, load modulation.**

I. Introduction

POWER amplifiers (PAs) are often required to provide wide-range dynamic output power control while maintaining high efficiency. The requirement of efficiency over a wide range of power levels is at odds with the dominant characteristics of most classes of PAs, which tend to have peak efficiency only under highly saturated, peak output power operation. In order to maintain high efficiency over a wide dynamic range, then, a promising approach is to exploit the saturated efficiency characteristic by continuing to operate in a saturated mode even as output power is modulated. Output power of a saturated PA can be controlled for example by modulating either the drain terminal, as in polar and envelope tracking techniques [1]–[3], modulation of the effective load impedance as in Doherty [4]–[6], outphasing [7]–[38], or direct load modulation [39]–[41] architectures, or through a combination of these approaches [42], [43]. In principle, the average modulated efficiency of these techniques is directly related to the extent to which saturated operation can be maintained. Of these architectures, therefore, outphasing with saturated PAs (or, in the ideal limit, switched-mode PAs) may represent the most readily achievable path to high efficiency over a wide power range, due to the wide operating range over which the multiple branch PAs can operate in saturation.

The outphasing approach employs phase-shift control of multiple branch amplifiers to modulate the power delivered to the load. When realized with a lossless power combining network [7]–[31], the branch PAs interact such that variations in their relative phases modulate the effective loading impedances, enabling phase-control of overall system output power. This technique is able to realize a wide dynamic range over which all branch PAs remain in an efficient saturated mode of operation.

A significant limitation in traditional approaches to outphasing, including in its original formulation proposed in the 1930's [7], is the substantial variation in the reactive component of the branch PAs' loading impedance that occurs across the outphasing range. This is an undesirable byproduct of the outphasing and power combining mechanism (which controls output power through modulation of the *real* component of the branch PA loading impedances). Subjecting the branch PAs to variable reactive loading tends to degrade efficiency performance due to both the sensitivity to loading conditions exhibited by most RF amplifiers (including switched-mode RF PAs), and added conduction losses associated with the reactive currents [17].

In order to address the suboptimal loading conditions of conventional outphasing formulations, a multi-way power combining and outphasing amplifier has been introduced that provides branch PA loading conditions that are almost entirely resistive over a wide output power range [8], [9]. Four-way implementations of this approach have been demonstrated using all lumped elements in a tree structure [9], [10], and by incorporating microstrip lines with ground-referenced shunt reactive elements [11], [12]. In [12] it was shown that these various realizations of the multi-way combining approach could be related through network transformations and shown to have identical theoretical port relationships. The preferred implementation for a particular application will therefore depend on power level and carrier frequency, and availability of appropriate passive components.

This work introduces a multi-way non-isolating power combining structure composed of transmission-line (TL) sections connected in a tree structure. By using only power-path trans-
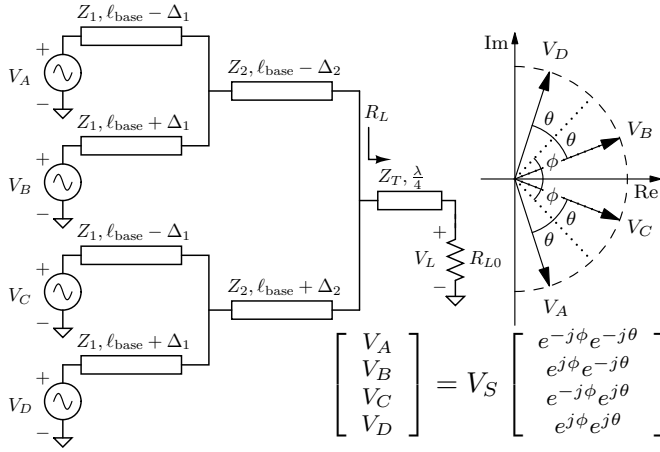
Fig. 1. Diagram of the four-way power combining network based on transmission line elements. The phase relationship among the four inputs to the PAs are also shown. The ideal voltage sources represent the four branch PAs.

mission lines, this structure eliminates the need for reactive elements, reducing parasitic effects due to ground return paths and allowing for more compact layout compared to the radial stub implementation in [12]. The proposed outphasing system is broadly related to those in [8]–[12], although it cannot be directly derived from them and has very different design and control considerations. The proposed approach shares the benefits of power combining techniques based on non-isolating transmission-line combiners [20], [26], [44], [45] while significantly reducing the reactive loading of the power amplifiers. This paper expands on the preliminary demonstration of this approach in the authors' conference paper [46] with a complete theoretical analysis of the transmission-line combining network. This work introduces the derivation of the input-port admittance characteristics and outphasing control strategies. We discuss the reasoning for the choice of base electrical length in the combiner design, and show a compact layout of the approach.

Section II of the paper presents the underlying theory for the proposed approach, including derivation of the input-port impedance and output power control characteristics of the multi-way transmission-line combining network, development of and a network design methodology. Section III presents two design examples of the network used in simulation-based and experimental validation of the approach. The remaining system components and experimental validation results of the four-way, 2.14-GHz prototype are described in Section IV. Section V concludes the paper.

II. THEORY

The four-way transmission-line-based power combining network is shown in Fig. 1. Eight-way and higher-order versions can be realized by extension of the techniques described in this work, but we have selected the four-branch version as having a balance of improved PA loading conditions and broad usefulness. As indicated in Fig. 1, the characteristic impedances of the branch transmission lines are Z_1 and Z_2

respectively. Each transmission line pair has a base length ℓ_{base} with a specified offset (Δ_1 or Δ_2) from that base length. In other words, the transmission-line lengths are chosen to have a increment/decrement in length from the base length. Although an arbitrary base length is possible, the base length is here chosen to be a quarter- or half-wavelength, as this allows for symmetric length increments $\pm\Delta_{1,2}$ and simplifies the combiner analysis. Practical considerations for selecting the base transmission-line length are discussed in Section III below.

Throughout the following analysis, we will assume that the four branch PAs operate as ideal voltage sources, as this is the ideal condition for outphasing systems [32]. In practice, candidate PA classes for implementation include those producing a constant output voltage amplitude independent of input amplitude; for example class E, saturated class B or class F amplifiers. We also make the simplifying assumption that the PA operating efficiency is directly proportional to the power factor of its effective loading impedance, as shown in [8] for ideal saturated class B PAs. As a result, this work seeks to maximize efficiency by minimizing the reactive component of the loading seen by the branch PAs. It is also noted that some types of switching amplifiers (including class E amplifiers) can be designed to work well across variable resistive loads, as described for example in [28], [47]. A consequence of this design goal is that the matching among the loading conditions of all four PAs is maximized. We note that if an alternate loading trajectory provides improved efficiency for a practical branch PA, the resistive loading trajectory presented in this work could be transformed to in such a way that all four branch PAs operate as closely to that desired trajectory as possible.

A. Input-Port Admittance Characteristics

Understanding the input-port admittance characteristics of the transmission-line (TL) combiner of Fig. 1 is important for its design and analysis. In other words, it is of interest to the designer to know how the effective loading of the PAs (due to the combiner) changes with outphasing. One convenient approach for determining these characteristics is to first describe the TL combiner with a multi-port admittance matrix relating the combiner input-port voltages to its respective input-port currents. Such a matrix captures the behavior of the combiner and allows one to easily derive the effective PA loading at any of the combiner input ports for an arbitrary set of PA outphasing angles. In the case of the four-way combiner of Fig. 1, this reduces to a four-port admittance matrix relating the four input-port voltages V_A - V_D to the respective input-port currents. Note that one can also describe the four-way combiner with a five-port admittance matrix, where the fifth port corresponds to the combiner's output port. In the following theoretical discussion, however, we choose to treat the output port along with its terminating load R_L as part of the combiner network, as it requires considerably less algebraic manipulation to arrive at the result.

To derive the admittance matrix of the four-way combiner, consider first the three-port network of Fig. 2. Both lines have impedance Z_0 and their base length ℓ_{base} can be selected
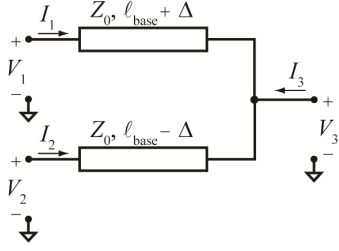
Fig. 2. A three-port network that represents a fundamental building block of the transmission-line-based combiner of Fig. 1. The two transmission lines each have a characteristic impedance Z_0 and a base line length ℓ_{base} which may be selected as an integer multiple of a quarter wavelength.

Fig. 3. Transmission line implementation of a two-way power combiner, showing the phase relationship of the input port voltages V_1 and V_2. The base length ℓ_{base} is selected as an integer multiple of a quarter wavelength. The characteristic line impedance Z_0 and the length increment Δ are design parameters. Z_L is the effective load as seen by the combiner and includes the effect of any additional impedance transformation stages.

as an integer multiple of a quarter wavelength. Furthermore, an integer number of half-wavelengths may be added to ℓ_{base} without changing the port characteristics. This three-port network of Fig. 2 can be thought of as a fundamental building block of multi-port transmission line combiners such as the one in Fig. 1. Conventional transmission-line analysis methods can be employed to show that the port voltages $V_1 - V_3$ and currents $I_1 - I_3$ for the three-port network of Fig. 2 with a half-wavelength base line length ($\ell_{\text{base}} = \lambda/2$) are related according to (1), where $\sigma = 2\pi\Delta/\lambda$ and $Y_{Z_0,\Delta}$ denotes the admittance matrix of the three-port network.

$$
\begin{bmatrix} I_1 \\ I_2 \\ I_3 \end{bmatrix} = Y_{(Z_0,\Delta)} \begin{bmatrix} V_1 \\ V_2 \\ V_3 \end{bmatrix}
$$

$$
= \frac{j}{Z_0 \sin(\sigma)} \begin{bmatrix} -\cos(\sigma) & 0 & -1 \\ 0 & \cos(\sigma) & 1 \\ -1 & 1 & 0 \end{bmatrix} \begin{bmatrix} V_1 \\ V_2 \\ V_3 \end{bmatrix} \quad (1)
$$

This admittance matrix can be employed in deriving the input-port admittance characteristics for multi-port transmission line combiners. For example, consider the two-way transmission-line combiner of Fig. 3 driving a load Z_L, in which the branch PAs are treated as ideal voltage sources V_1 and V_2. The sources are outphased as illustrated in the phasor diagram of Fig. 3. We can express the port voltages and currents using the matrix representation given by (2), where $Y_{(Z_0,\Delta)}$ is the admittance matrix (1) for the three-port network of Fig. 2.

$$
\begin{bmatrix} I_1 \\ I_2 \\ -I_L \end{bmatrix} = Y_{(Z_0,\Delta)} \begin{bmatrix} V_1 \\ V_2 \\ V_L \end{bmatrix}, \qquad V_L = Z_L I_L \quad (2)
$$

Solving (2) yields the relationship between the input-port voltages V_1 and V_2 and currents I_1 and I_2 given by (3) for the two-way combiner with half-wavelength base length, where $\sigma = 2\pi\Delta/\lambda$ and $\zeta = \cos(\sigma)\sin(\sigma)$.

$$
\begin{bmatrix} I_1 \\ I_2 \end{bmatrix} = \frac{Z_L}{Z_0^2 \sin^2(\sigma)} \begin{bmatrix} 1 - j\frac{Z_0}{Z_L}\zeta & -1 \\ -1 & 1 + j\frac{Z_0}{Z_L}\zeta \end{bmatrix} \begin{bmatrix} V_1 \\ V_2 \end{bmatrix} \quad (3)
$$

Furthermore, if one assumes that the PAs driving the two-way combiner are outphased according to the phasor diagram in Fig. 3, and the combiner input-port voltages have identical
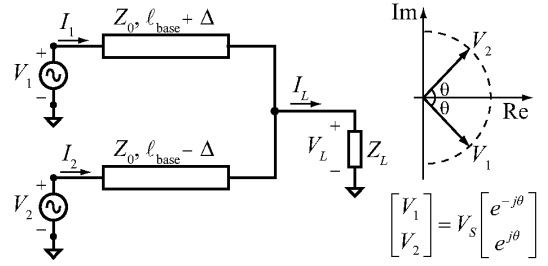
magnitude V_S (at the operating frequency at which the combiner is designed to operate), then (3) can be solved to yield the effective combiner input admittances $Y_{\text{eff},1} = I_1/V_1$ and $Y_{\text{eff},2} = I_2/V_2$, i.e., the admittance that each of the PAs sees looking into the combiner with all sources being active. It can be shown that $Y_{\text{eff},1}$ and $Y_{\text{eff},2}$ are complex conjugate pairs and are given by (4), where $\gamma = Z_L/Z_0$.

$$
Y_{\text{eff},1} = Y_{\text{eff},2}^* = \frac{\csc^2(\sigma)}{Z_0} \left[-\frac{\sin(2\sigma)\sin(\theta)}{2} \right.
$$
$$
\left. -j\left(\frac{\sin(2\sigma)\cos(\theta)}{2} + 2\gamma\sin(\theta) \right) \right] \quad (4)
$$

It can be shown for the two-way combiner of Fig. 3 that for a given PA output amplitude V_S, maximum power is delivered to the load Z_L when V_1 and V_2 are 180° out-of-phase, i.e., $V_1 = -V_2$. Interestingly, as can be seen from the admittance matrix (1) of this combining network, the load current I_L is independent of Z_L and is only a function of the input port voltages and the length of the transmission lines. This suggests that one can also regard the two-way combining network as an impedance transformation network with a differential input and a single-ended output that converts a differential input voltage $V_1 - V_2$ to an output current I_L according to (1). This network acts as a differential-input, single-ended-output immittance converter, in that it converts an input voltage to an output current (or an input current to an output voltage). In this regard it is similar to other impedance transformation networks such as the well-known quarter-wavelength transformer and its equivalent lumped-element counterparts [48]. Similar to other impedance transformation networks, the power loss exhibited by the network in Fig. 3 (owing to parasitic resistance, dielectric loss, etc.) also increases with the impedance transformation ratio.

An approach analogous to the one used for the two-way combiner can be employed for deriving the input-port characteristic of the four-way transmission-line combiner. Consider Fig. 4 representing the four-way combiner of Fig. 1 as a cascade of three-port networks, each with its respective admittance matrix $Y_{(Z_1,\Delta_1)}$ and $Y_{(Z_2,\Delta_2)}$. The node voltages $V_A - V_F$ and branch currents $I_A - I_F$ along with the load voltage V_L and current I_L can be related according the linear system
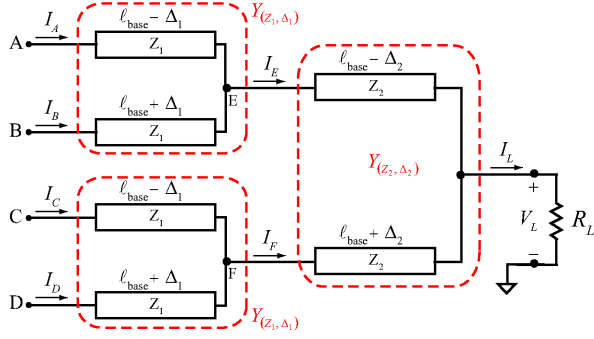
Fig. 4. Transmission-line-based four-way power combiner of Fig. 1 represented as a cascade of the three-port networks shown in Fig. 2. Each of the three-port networks is completely characterized by its corresponding admittance matrix Y. This is one possible approach for deriving the input-port admittance characteristic of the four-way combiner, and it can be similarly employed in the analysis of combiners with more than four input ports.

of equations (5a)-(5d) which can in turn be solved to yield the input-port admittance matrix $Y_{4\text{way}}$ for the four-way combiner with a half-wavelength line base length as given by (6), where $\sigma_1 = 2\pi\Delta_1/\lambda$, $\sigma_2 = 2\pi\Delta_2/\lambda$, $\gamma = R_L/Z_1$, and $\beta = Z_2/Z_1$.

$$\begin{bmatrix} I_B \\ I_A \\ -I_E \end{bmatrix} = Y_{(Z_1,\Delta_1)} \begin{bmatrix} V_B \\ V_A \\ V_E \end{bmatrix} \tag{5a}$$

$$\begin{bmatrix} I_D \\ I_C \\ -I_F \end{bmatrix} = Y_{(Z_1,\Delta_1)} \begin{bmatrix} V_D \\ V_C \\ V_F \end{bmatrix} \tag{5b}$$

$$\begin{bmatrix} I_F \\ I_E \\ -I_L \end{bmatrix} = Y_{(Z_2,\Delta_2)} \begin{bmatrix} V_F \\ V_E \\ V_L \end{bmatrix} \tag{5c}$$

$$V_L = R_L I_L \tag{5d}$$

$$\begin{bmatrix} I_A \\ I_B \\ I_C \\ I_D \end{bmatrix} = Y_{4\text{way}} \begin{bmatrix} V_A \\ V_B \\ V_C \\ V_D \end{bmatrix} = Y_0 \begin{bmatrix} M_1 & M_2 \\ M_2 & M_3 \end{bmatrix} \begin{bmatrix} V_A \\ V_B \\ V_C \\ V_D \end{bmatrix} \tag{6a}$$

$$Y_0 = \frac{\csc^2(\sigma_1)}{Z_1} \tag{6b}$$

$$M_1 = \begin{bmatrix} \gamma\sec^2\sigma_2 + j(\cos\sigma_1\sin\sigma_1 - \beta\tan\sigma_2) \\ -\gamma\sec^2\sigma_2 + j\beta\tan\sigma_2 \end{bmatrix}$$
$$\begin{matrix} -\gamma\sec^2\sigma_2 + j\beta\tan\sigma_2 \\ \gamma\sec^2\sigma_2 - j(\cos\sigma_1\sin\sigma_1 + \beta\tan\sigma_2) \end{matrix} \tag{6c}$$

$$M_2 = \begin{bmatrix} \gamma\sec^2\sigma_2 & -\gamma\sec^2\sigma_2 \\ -\gamma\sec^2\sigma_2 & \gamma\sec^2\sigma_2 \end{bmatrix} \tag{6d}$$

$$M_3 = \begin{bmatrix} \gamma\sec^2\sigma_2 + j(\cos\sigma_1\sin\sigma_1 + \beta\tan\sigma_2 \\ -\gamma\sec^2\sigma_2 - j\beta\tan\sigma_2 \end{bmatrix}$$
$$\begin{matrix} -\gamma\sec^2\sigma_2 - j\beta\tan\sigma_2 \\ \gamma\sec^2\sigma_2 - j(\cos\sigma_1\sin\sigma_1 - \beta\tan\sigma_2) \end{matrix} \tag{6e}$$

Note that the admittance matrix in (6) provides a complete description of the input-port characteristics of the four-way combiner of Fig. 1. It allows one to determine the input-port currents $I_A - I_D$ for any arbitrary set of input-port voltages $V_A - V_D$ and vice versa.

For the four-way combiner of Fig. 1, if one further assumes that the PAs are outphased according the phasor relationship in Fig. 1 with all input-port voltages $V_A - V_D$ having the same magnitude V_S (at the combiner operating frequency), then one can solve (6) for the effective admittance $Y_{\text{eff},A} - Y_{\text{eff},D}$ each of the PAs sees looking into the combiner as a function of the outphasing angles θ and ϕ with all other PAs active. As can be seen from (7), $Y_{\text{eff},A}$ and $Y_{\text{eff},D}$, as well as $Y_{\text{eff},B}$ and $Y_{\text{eff},C}$ are complex conjugate pairs. It is important to note that (7) gives the effective input admittance at the combiner's input ports assuming that the PAs are outphased according to Fig. 1 and the PA output voltages have equal magnitudes. Furthermore, (7) is derived for a four-way combiner with transmission-lines having half-wavelength base length ($\ell_{\text{base}} = \lambda/2$ in Fig. 1). An identical approach can be used to arrive at the effective input admittance equations for a combiner constructed with transmission lines having quarter-wavelength base length (see Appendix A).

B. Output Power Control

Control of the output power delivered by the combiner to the load can be achieved either by adjusting the signal amplitudes V_S of the combiner inputs (through modulation of the PA drive amplitudes and/or their supply voltages), by controlling the phase shift between the PAs (phase modulation), or by a combination of both of these methods. To derive an expression for the power at the output of the combiner as a function of the phase shift between the PAs and their output voltage amplitudes, consider again Fig. 4. It can be readily shown through conventional transmission line theory that for the four-way combiner with half-wavelength transmission-line base length, the load current I_L depends on the branch currents I_E and I_F as per (8), where $\sigma_2 = 2\pi\Delta_2/\lambda$ (see Fig. 1).

$$I_L = -\sec(\sigma_2)[I_E + I_F] \tag{8}$$

Furthermore, from (1), (5a) and (5b), one can express the branch currents I_E and I_F in terms of the combiner's input-port voltages $V_A - V_D$ according to (9), where $\sigma_1 = 2\pi\Delta_1/\lambda$.

$$\begin{bmatrix} I_E \\ I_F \end{bmatrix} = -\frac{j}{Z_1\sin\sigma_1} \begin{bmatrix} 1 & -1 & 0 & 0 \\ 0 & 0 & 1 & -1 \end{bmatrix} \begin{bmatrix} V_A \\ V_B \\ V_C \\ V_D \end{bmatrix} \tag{9}$$

Combining (8) and (9), the combiner's load current I_L can be written as per (10). Note that (10) allows one to calculate the combiner's load current (for $\ell_{\text{base}} = \lambda/2$ in Fig. 1) for an arbitrary set of input-port voltages $V_A - V_D$. Furthermore, by assuming that the all the PAs have equal output voltage amplitudes V_S and phase relationships as per Fig. 1, (10) can be simplified to obtain the combiner's load current (11) in

$$Y_{\text{eff},A} = \frac{\csc^2 \sigma_1 \sec^2 \sigma_2}{Z_1} \left[\sin\phi(-\beta\cos\phi\sin 2\sigma_2 + 4\gamma\cos\theta\sin(\theta+\phi)) \right.$$
$$\left. + j(\cos\sigma_1\cos^2\sigma_2\sin\sigma_1 + \sin^2\phi(2\gamma\sin 2\theta - \beta\sin 2\sigma_2) - 2\gamma\cos^2\theta\sin 2\phi) \right] \quad (7a)$$

$$Y_{\text{eff},B} = \frac{\csc^2 \sigma_1 \sec^2 \sigma_2}{Z_1} \left[2\sin\phi(-2\gamma\cos\theta\sin(\theta-\phi) + \beta\cos\phi\sin\sigma_2\cos\sigma_2 \right.$$
$$\left. -j(\cos\sigma_1\cos^2\sigma_2\sin\sigma_1 + \sin\phi(-4\gamma\cos\theta\cos(\theta-\phi) + \beta\sin 2\sigma_2\sin\phi)) \right] \quad (7b)$$

$$Y_{\text{eff},C} = \frac{\csc^2 \sigma_1 \sec^2 \sigma_2}{Z_1} \left[2\sin\phi(-2\gamma\cos\theta\sin(\theta-\phi) + \beta\cos\phi\sin\sigma_2\cos\sigma_2 \right.$$
$$\left. +j(\cos\sigma_1\cos^2\sigma_2\sin\sigma_1 + \sin\phi(-4\gamma\cos\theta\cos(\theta-\phi) + \beta\sin 2\sigma_2\sin\phi)) \right] \quad (7c)$$

$$Y_{\text{eff},D} = \frac{\csc^2 \sigma_1 \sec^2 \sigma_2}{Z_1} \left[\sin\phi(-\beta\cos\phi\sin 2\sigma_2 + 4\gamma\cos\theta\sin(\theta+\phi)) \right.$$
$$\left. -j(\cos\sigma_1\cos^2\sigma_2\sin\sigma_1 + \sin^2\phi(2\gamma\sin 2\theta - \beta\sin 2\sigma_2) - 2\gamma\cos^2\theta\sin 2\phi) \right] \quad (7d)$$

---

terms of the PA outphasing angles θ and ϕ, and their output amplitude V_S.

$$I_L = j\frac{\sec\sigma_2}{Z_1\sin\sigma_1}(V_A + V_C - V_B - V_D) \quad (10)$$

$$I_L = \frac{4V_S\sin\phi\cos\theta}{Z_1\cos\sigma_2\sin\sigma_1} \quad (11)$$

The output power P_{out} delivered by the combiner to the load can be easily calculated from (11), and is given by (12) for the four-way combiner of Fig. 1 with half-wavelength transmission-line base length. Z_1 is the characteristic impedance of the input-branch transmission lines, R_L is the effective combiner load (after any impedance transformation stages), θ and ϕ are the PA outphasing angles, and σ_1 and σ_2 are given by $2\pi\Delta_1/\lambda$ and $2\pi\Delta_2/\lambda$, respectively. Using a similar approach, the output power equation in the case of a combiner with quarter-wavelength transmission-line base length can be developed (see Appendix A). Note that (12) relies on the assumption that the combiner's input-port voltages are purely sinusoidal (at the frequency at which the combiner is designed to operate) with identical amplitudes V_S as per the phasor representation shown in Fig. 1.

$$P_{out} = \frac{I_L^2 R_L}{2} = \frac{8R_L V_S^2}{Z_1^2 \sin^2\sigma_1\cos^2\sigma_2}\sin^2\phi\cos^2\theta \quad (12)$$

As can be seen from (12), one can indeed modulate the output power by either controlling the PA outphasing angles θ and ϕ, and/or by modulating the output voltage amplitude V_S of the PAs. The output signal's phase is simply controlled by applying a common phase offset to all four of the inputs V_A–V_D. The variation of output power as a function of the outphasing angles is shown in the contour plot of Fig. 5. This figure highlights that a given output power can be produced by multiple outphasing angle pairs $[\theta, \phi]$, allowing for design freedom in how the control angles are chosen. This observation forms the basis of the outphasing control strategy described in the next section, in which we use additional criteria (e.g.,
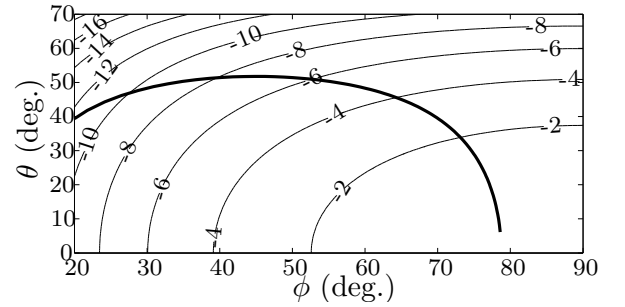

Fig. 5. Output power contours (normalized to peak power, lines 2 dB apart), when the outphasing control angles are varied. Because a given output power can be generated by multiple combinations of phase control angles, we can impose additional design criteria on how the control angles are selected. In this work, we choose to minimize the reactive component of the effective loading impedance on the four branch PAs, thus maximizing efficiency. The outphasing angle trajectory corresponding to this control law is shown.

minimizing reactive loading components) to select the control law. The characteristics of this combiner are further explored in Appendix B.

C. Outphasing Control Strategies

As can be seen from the output power relation derived in (12) and Fig. 5, there exist infinite number of PA outphasing angle pairs $[\theta, \phi]$ for a given combiner output power P_{out}. This extra degree of freedom allows us to impose additional criteria on the input-port characteristics of the combiner so as to achieve the specified branch PA loading conditions with modulation of output power. In this paper, we choose to minimize the reactive loading through selection of an optimal susceptance (OS) control law: the PA outphasing angles θ and ϕ are chosen such that the peak imaginary part of the load admittance is minimized over a specified output power operating range.

The OS control angles for a given combiner output power level can be calculated by employing (12) and simultaneously minimizing the susceptive components of the combiner's effective input admittances $Y_{\text{eff},A} - Y_{\text{eff},D}$ given in (7). Interestingly, it can be shown that for a given output power P_{out}, minimizing the susceptive components of the combiner's effective input admittances $\text{Im}(Y_{\text{eff},A}) - \text{Im}(Y_{\text{eff},D})$ corresponds to all four susceptive components having identical magnitudes, i.e., $|\text{Im}(Y_{\text{eff},A})| = |\text{Im}(Y_{\text{eff},B})| = |\text{Im}(Y_{\text{eff},C})| = |\text{Im}(Y_{\text{eff},D})|$. Thus, to determine the OS control angles, we must solve the output power relation in (12) for θ and ϕ while simultaneously forcing identical susceptive magnitudes of the combiner's effective input admittances given by (7). For the four-way combiner of Fig. 1 with half-wavelength transmission-line base lengths, these two conditions reduce to the system of equations in (13), where (13a) follows from requiring identical input susceptance magnitudes, while (13b) is a rearranged form of (12).

$$\frac{Z_1 \sin(2\sigma_1)\cos^2(\sigma_2)}{4R_L} = \sin(2\phi)\cos^2(\theta) \qquad (13a)$$

$$\frac{P_{out} Z_1^2 \sin^2(\sigma_1)\cos^2(\sigma_2)}{8R_L V_S^2} = \sin^2(\phi)\cos^2(\theta) \qquad (13b)$$

The system of equations in (13) can be further solved to yield the OS control angles θ and ϕ for the four-way combiner of Fig. 1 with $\ell_{\text{base}} = \lambda/2$ as per (14) and (15), where $\sigma_1 = 2\pi\Delta_1/\lambda$, $\sigma_2 = 2\pi\Delta_2/\lambda$ and P_{out} is the output power delivered by the combiner to the load R_L.

$$\phi = \arctan\left(\frac{Z_1 \tan(\sigma_1)P_{out}}{2V_S^2}\right) \qquad (14)$$

$$\theta = \arccos\left(\cos\sigma_2 \cos\sigma_1 \sqrt{\frac{4V_S^4 + P_{out}^2 Z_1^2 \tan^2\sigma_1}{8R_L V_S^2 P_{out}}}\right) \qquad (15)$$

The calculated load admittances seen by the four branch PAs are shown in Fig. 6 for an example design with a 10:1 operating power range and $Z_1 = Z_2 = 3R_L$. Indeed, as can be seen from Fig. 6, the magnitude of the susceptive loading of all four PAs is identical, which is in agreement with the criteria on which the derivation of OS control is based. Furthermore, as predicted by (7), the loading admittance of PA pairs A and D, and B and C are complex conjugates. Referring to Fig. 6, one can notice that due to the OS control, the four PAs are loaded with nearly identical conductances, and hence they contribute evenly to the overall power delivered to the load.

Although different, this transmission-line-based multi-way outphasing system has properties that are somewhat analogous to those with the multi-way combining network in [8], [9] and its variations [11], [12]. A comparison of the theoretical effective loading conditions for Chireix combining, lumped-element four-way [10], and transmission-line-based four-way combining is shown in Fig. 7 for example combiner designs of similar dynamic ranges. It can be seen that when these systems are synthesized with power amplifiers sensitive to loading reactance, there is a substantial advantage to four-way combining. Selection between the transmission-line four-way combiner and the discrete four-way combiner (and its
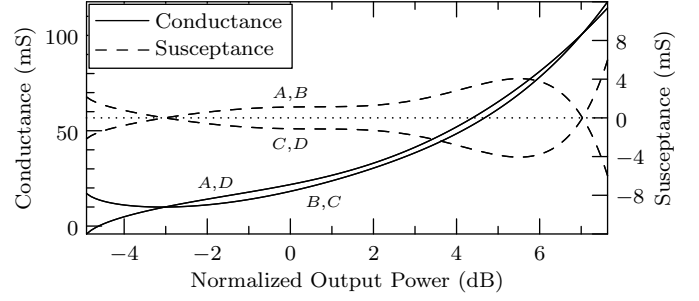

Fig. 6. Loading conditions for the branch PAs calculated at the input to the four-way TL combiner with $Z_1 = Z_2 = 100\ \Omega$, $\ell_{\text{base}} = \lambda/2$, $\Delta_1 = 0.049\lambda$ and $\Delta_2 = 0.054\lambda$, $Z_T = 40.8\ \Omega$, $R_{L0} = 50\ \Omega$, and $R_L = 33\ \Omega$ (see topology in Fig. 1). Power is normalized to the power delivered when all four PAs drive 50-Ω loads.
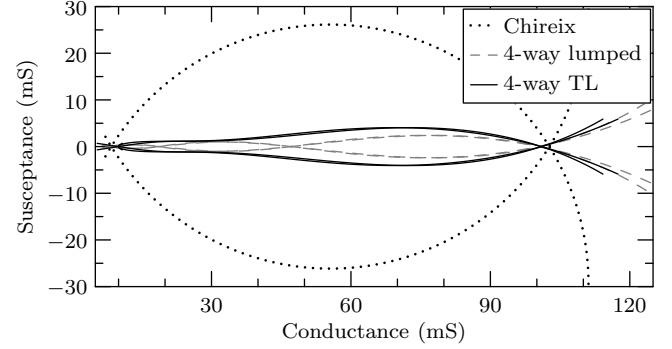

Fig. 7. Comparison of loading conditions for example outphasing systems, implemented with conventional Chireix combining, lumped-element 4-way [12], and transmission-line-based 4-way combining with $Z_1 = Z_2 = 3R_L$ (this work).

microstrip variations) will depend primarily on ease of implementation (e.g., with respect to carrier frequency, loss and layout considerations).

D. Combining Network Design

The combining network is designed based on a specification of its load resistance R_L and its operating output power range. For this analysis, we consider the operating output power range to be delineated by the highest and lowest output power values at which the imaginary component of the effective load impedances seen at the combiner input are zero. For instance, for the example values given in Fig. 6, the output power range is 10 dB, based on the separation (in normalized output power) between the two zero-susceptance points. In practice, the usable operating range may be slightly larger than this value; for instance in Fig. 6 the susceptance to below -4 dB normalized output power is still below the peak susceptance level over the nominal operating range.

The ratio of the transmission line impedances to the load resistance R_L determines the magnitude of the load susceptance variations seen by the branch PAs, and the overall range over which the combiner can optimally operate. Generally, these impedances should be chosen to be at least twice R_L to limit the variation in loading susceptance. The larger the ratio of Z_1 and Z_2 to R_L, the smaller the range of susceptance, but the output power range over which susceptance stays small
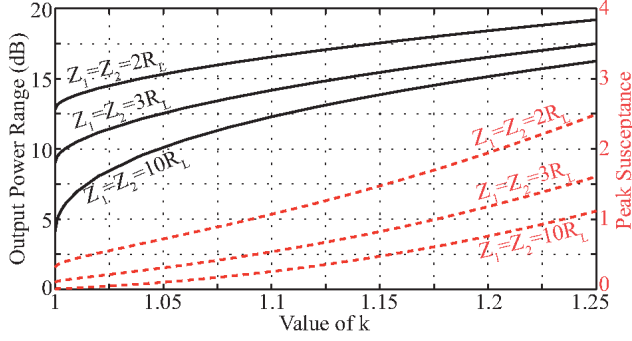
Fig. 8. Design curves showing the output power range (solid) and peak susceptance (dashed) for the proposed transmission-line combiner with transmission-line characteristic impedances $Z_1 = Z_2$ selected as 2, 3, and 10 times R_L. The peak susceptance axis shows values normalized to $R_L = 1\Omega$; to denormalize, multiply values by $1/R_L$.
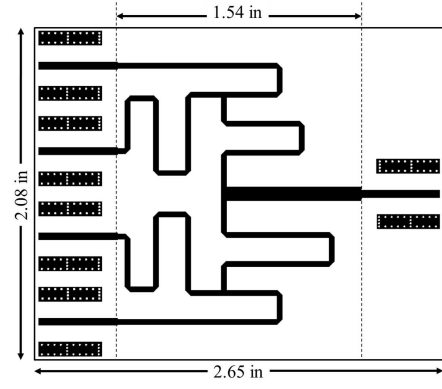

Fig. 9. Layout of the compact four-way power combiner. The PCB is designed for a 2.14-GHz carrier frequency and measures 52.8 mm by 67.3 mm, with the core combiner layout only 39.1 mm wide.

is also reduced. Conversely, for smaller ratios a larger power range can be achieved, but at the expense of greater susceptive components. Practical considerations and implementation details may further constrain the range of possible values for Z_1 and Z_2.

The design curves in Fig. 8 are used to determine appropriate values for Z_1 and Z_2, based on a desired load resistance R_L, output power range (in dB), and peak susceptance for a specified design. Note that these curves assume equal values for the transmission line impedances Z_1 and Z_2. An intermediate (unitless) design parameter uniquely characterizing the combiner is denoted as k. Given a desired output power range, the value for k can be found by tracing across from the "Output Power Range" axis to the appropriate black (solid) curve corresponding to the desired ratio $Z_1 = Z_2$ to R_L. The abcissa then denotes the appropriate k value for the design. Based on this value, the resulting peak susceptive PA loading can be read off the right axis (red, dashed curves). Having selected the value for k, the length increments Δ_1 and Δ_2 are computed according to (16)-(17) for the combiner having a base-length $\lambda/2$. For the combiner with $\lambda/4$ base length, inverse cosine functions replace the the inverse sine functions in these equations.

$$\Delta_1 = \frac{\lambda}{2\pi} \sin^{-1} \left(\frac{2R_L}{(k+1)(k+\sqrt{k^2-1})Z_1} \right) \qquad (16)$$

$$\Delta_2 = \frac{\lambda}{2\pi} \sin^{-1} \left(\frac{2R_L}{(k+1)Z_2} \right) \qquad (17)$$

The load resistance R_L used in the combiner network design may represent a different load value connected via an impedance transformer, such as the $\lambda/4$, Z_T line indicated in Fig. 1. This impedance transformer stage provides an additional degree of control over the transmission line characteristic impedances, for example to improve the manufacturability of the design. As shown in Fig. 1, we denote the actual load resistance as R_{L0}, and the design resistance as R_L.
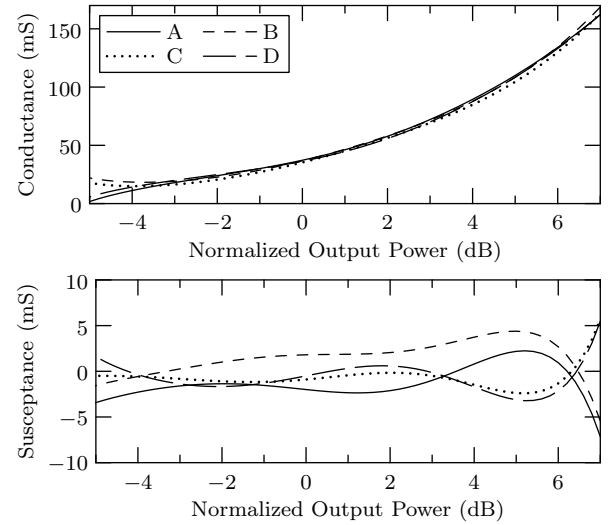
Fig. 10. Simulated loading impedances when the extracted layout is driven using ideal voltage sources.

III. COMBINER DESIGN AND IMPLEMENTATION

This section presents two design examples of the four-way combining network, both for implementation on Rogers 4350 substrate and operation at 2.14 GHz with an approximately 10-dB power range for outphasing control. Both designs utilize $\ell_{\text{base}} = \lambda/2$ due to practical layout limitations associated with the required Δ_1 and Δ_2 values. Transmission line and load impedances are likewise selected based on manufacturability considerations. The first example is designed for a compact layout, while the second accomodates port spacing requirements specific to the experimental system.

A. Compact Layout Example

Following the methodology outlined in Section II, we select a value of $k = 1.01$ for the design parameter based on the $Z_1 = Z_2 = 3R_L$ curve in Fig. 8 and a specified 10-dB power range. This compact layout example is designed for a 20-mil thick Rogers 4350 substrate, so in order for the values of R_L and $Z_1 = Z_2$ to result in practical dimensions we have
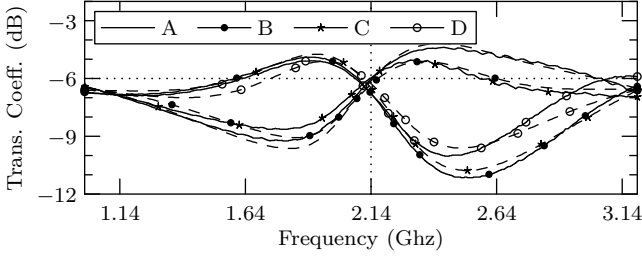
Fig. 11. Comparison of simulated (dashed) and measured (solid) transmission coefficient magnitudes for the compact combiner layout when all ports are 50-Ω terminated.
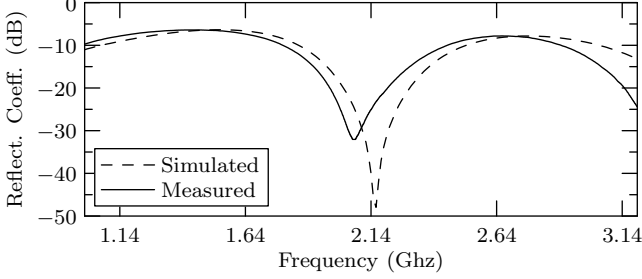

Fig. 12. Comparison of simulated and measured reflection coefficient at the combiner output port when all ports are 50-Ω terminated.

Fig. 13. Relative phases measured at the compact combiner's input ports when all ports are 50-Ω terminated and the output port is driven. The expected relative phases at 2.14 GHz based on the outphasing control law used in this work are indicated by the horizontal dashed lines.

Fig. 14. Photo of the 100 W, 2.14 GHz experimental system. The branch PAs, also used in the experimental system of [12], are based on [5]. The PA carriers in this connectorized prototype require spacing of at least 81.3 mm between the input ports, causing the relatively large combining network layout shown.

chosen values $R_L = 20$ Ω and $Z_1 = Z_2 = 60$ Ω. The design resistance $R_L = 20$ Ω is matched to the desired 50-Ω load (R_{L0}) through a quarter-wave line with $Z_T = 31.6$ Ω.

The transmission-line length increments for this design are computed according to (16)-(17) as $\Delta_1 = 0.047\lambda$ and $\Delta_2 = 0.054\lambda$, where $\lambda \approx 3490$ mils at 2.14 GHz for this substrate. With these values determined, the layout is implemented and simulated using Agilent Advanced Design Systems (ADS) software. Mitered bends are used to create the compact serpentine layout shown in Fig. 9, and spacing between the branches is kept above 3x the microstrip line widths to minimize coupling among the branches [49]. An additional design constraint is to locate all four inputs on a single edge of the printed circuit board opposite to the single output port, as shown. The compact combiner PCB for a 2.14-GHz carrier measures only 52.8 mm by 67.3 mm, with the core combiner layout (that is, omitting the 50-Ω interconnects) only 39.1 mm wide.

The compact combiner is characterized in simulation by using Momentum RF to extract an EM model of the core layout. When this extracted layout model is simulated as a combining structure driven by four ideal branch PAs and with an ideal 50-Ω load, the simulated loading conditions are as shown in Fig. 10. The performance closely matches that of the ideal system (see Fig. 6), with the magnitude of the imaginary component of the load remaining under 5 mS over the range of operation.

The extracted combiner was fabricated on 20-mil thick Rogers 4350 substrate and its port relationships were characterized using a four-port Rohde & Schwarz ZVA67. Figs. 11 and 12 show the simulated and measured frequency response
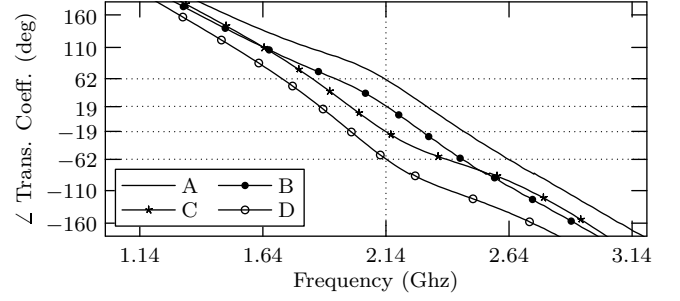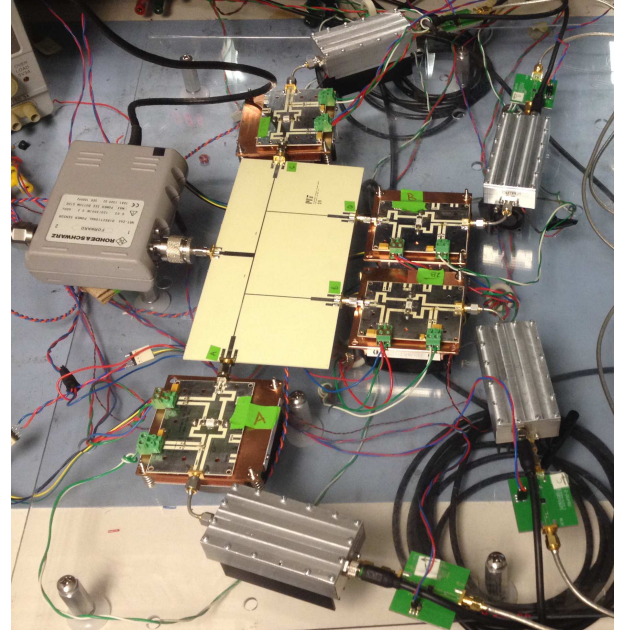
of the four transmission coefficients $|S_{15}|$–$|S_{45}|$ (where port 5 is the output/combining port) and the output port reflection coefficient $|S_{55}|$ when all ports are 50-Ω terminated. The phase of transmission coefficients S_{15}–S_{45} is shown in Fig. 13; the relative phases at the four ports corresponds to the expected outphasing relationship for this design (shown as dashed lines) at 2140 MHz within ±1.5 degrees. From these measured results, it can be seen that operation of this compact combiner design should be possible over at least 200 MHz bandwidth.

B. Experimental Prototype Layout

The experimental system has physical constraints that prevent the use of the compact layout described in the section above. In particular, the branch PAs are mounted on carriers that require spacing of at least 81.3 mm between input ports. In order to experimentally validate the approach (using the same
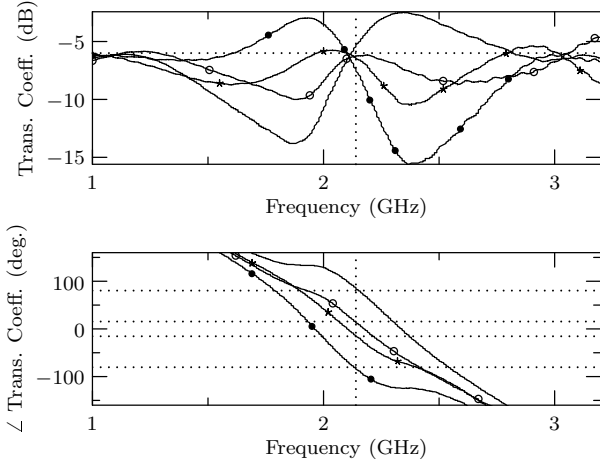
Fig. 15. Measured transmission coefficients at the input ports of the combiner used in the experimental setup, when all ports are 50-Ω terminated and the combiner output port is driven.
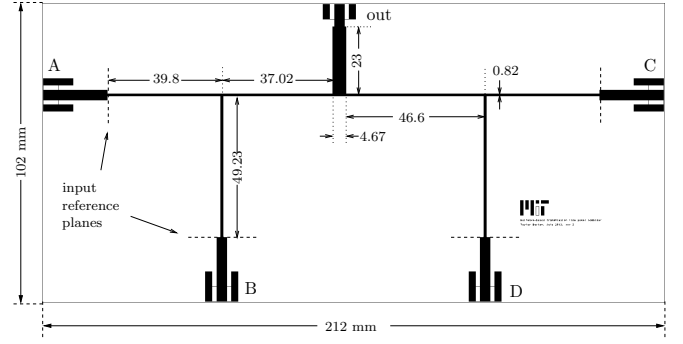

Fig. 16. Annotated layout of the experimental combining network, with dimensions given in mm. The board is implemented on 1.52-mm thick Rogers 4350 substrate. (Figure reproduced from [46].)

power amplifiers as for previous outphasing systems [10]–[12] for comparison purposes), therefore, a second prototype combiner was designed using the "T" structure layout shown in Fig. 14.

This design uses $Z_1 = Z_2 = 100\ \Omega$, $\ell_{\mathrm{base}} = \lambda/2$, $\Delta_1 = 0.049\lambda$ and $\Delta_2 = 0.054\lambda$. (Note that the related conference paper [46] indicated values $\Delta_1 = 0.201\lambda$ and $\Delta_2 = 0.196\lambda$ in error; the lengths $\Delta_1 = 0.049\lambda$ and $\Delta_2 = 0.054\lambda$ were used.) A quarter-wave transformer with $Z_T = 40.8\ \Omega$ functions as an impedance transformer between the $R_L = 33\ \Omega$ design resistance and the actual $R_{L0} = 50\ \Omega$ load. A 1.52-mm RO4350 substrate was selected as yielding manufacturable dimensions sizes for the 100-Ω and 40.8-Ω lines. The combiner's "T" junction structure was chosen to accomodate the larger layout requirements (specifically, the spacing between PAs evident in Fig. 14). Note, however, that the asymmetry in the input paths with respect to the T junctions is not ideal and that the compact layout version above will perform more closely to the ideal combiner due to the symmetry of the junctions.

An additional practical constraint relates to the net electrical length of the RF path connecting the PA (specifically, the drain of the device) and the combiner. In order for the resistive load modulation at the combiner to appear resistive at the device, this net electrical length must be an integer multiple of quarter wavelengths. Additional 50-Ω lines are included on the combiner board to augment the microstrip lengths on the power amplifier PCB and the interconnects themselves to reach the desired total length. The final dimensions of this combiner implementation are 212 mm by 102 mm, substantially larger than the compact version described in the previous section. Detailed dimensions of the experimental combining network are given in Fig. 16.

As described in [10], multi-way combiners may be characterized through reverse drive (operating the combiner as a splitter and measuring the response). When the system was measured by driving the output port (with the four input ports terminated with 50 ohms), the port magnitude match was found to be within $\pm5\%$ in voltage amplitude of an ideal (even) split, and the phase within $3°$ of the expected values. The measured transmission coefficients are shown in Fig. 15.

C. Quarter-Wave Base Length Design Example

As described in Section II, it is possible to select either a quarter-wavelength or half-wavelength as the base length for the power combining network. Because a shorter transmission-line length will have lower insertion loss, it may seem preferable to use a quarter-wavelength base. For our design constraints, however (operating frequency, desired loading impedance for the branch PAs, design choice for k), we found that the quarter-wavelength results in impractically short line lengths.

Consider, for example, implementing a combiner as in the compact layout example in Section III-A, with $k = 1.01$, $Z_1 = Z_2 = 3R_L = 60\ \Omega$, and design load resistance value $R_L = 20\ \Omega$. Replacing the inverse sine functions in (16)–(17) and evaluating with the above values yields $\Delta_1 = 0.2035\lambda$ and $\Delta_2 = 0.1962\lambda$. The long and short line lengths for stages 1 and 2 are therefore:

$$\ell_{\mathrm{base}} + \Delta_1 = 0.4535\lambda \qquad \ell_{\mathrm{base}} - \Delta_1 = 0.0465\lambda \qquad (18)$$

$$\ell_{\mathrm{base}} + \Delta_2 = 0.4462\lambda \qquad \ell_{\mathrm{base}} - \Delta_2 = 0.0538\lambda \qquad (19)$$

For our substrate, the shortest of these four lengths would be on the order of 3.6 mm, compared to the longest which is approximately 25.8 mm, making layout challenging.

As k becomes larger, the terms inside the parentheses for (16)–(17) become smaller. In the half-wavelength-based combiner, this means that as k increases the difference lengths Δ_1 and Δ_2 become small, and may present a different kind of manufacturing challenge in distinguishing between the two different path lengths. In this case, the quarter-wavelength-based design may be preferred if the operating frequency allows for lengths corresponding to small fractions of a wavelength.

IV. MEASURED SYSTEM PERFORMANCE

A. Experimental Setup

Fig. 14 shows a photograph of the experimental RF outphasing amplifier. The branch PAs are based on the inverse
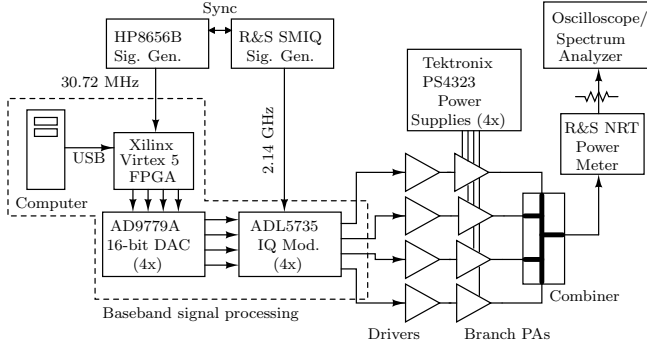
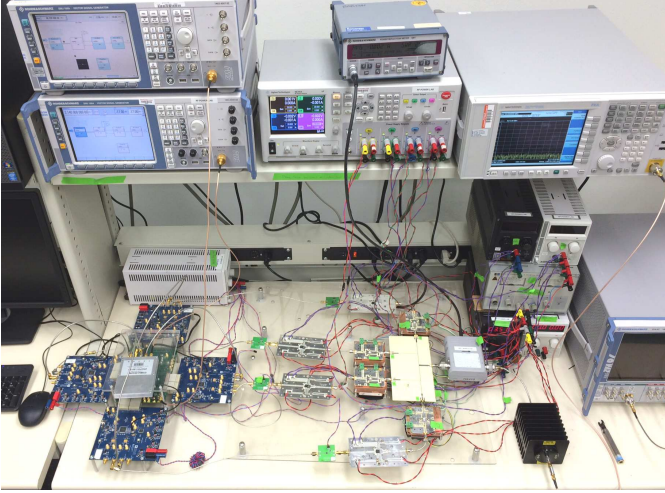Fig. 17. Block diagram of the experimental measurement setup.

Fig. 18. Photograph of an approximation of the experimental setup, recreated to show the test bench.

class F design in [5], discussed in greater detail in [11]. Signal component separation is performed in MATLAB on a PC, and an FPGA provides an interface between the PA and four digital-to-RF upconverting paths based on Analog Devices AD9779A DACs and ADL5735 IQ modulators as shown in the block diagram in Fig. 17. (Note that an analog signal component separation approach could also be realized in place of the multiple digital-to-RF paths, as described in [30], [31], though that was not done in this work.) Output power is measured with a Rohde & Schwarz NRT-Z44 through power meter. The setup allows for CW measurements of the four-way power combining system output power and drain efficiency. Due to memory limitations on the FPGA, however, the testbench has limited ability to perform modulated tests (as described in greater detail in [12]). A recreation of the experimental testbench is shown in Fig. 18.

B. CW System Performance

The system CW outphasing performance is characterized by varying both amplitude and relative phases of the four CW branch PA inputs. As in the related system described in [12], the signal component separation algorithm to determine the four branch PAs input signals is based on a combination of
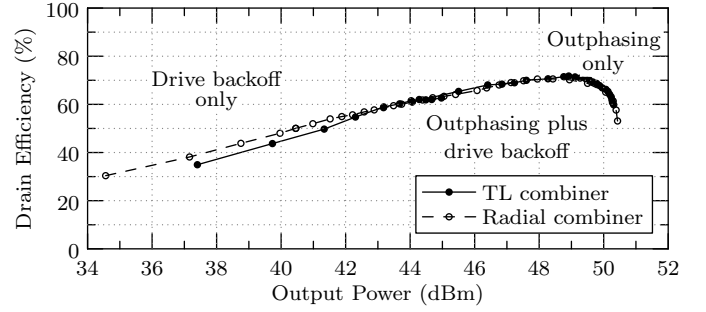

Fig. 19. CW measurements of the drain efficiency and output power when the outphasing angles are swept, and comparison to measurements of the radial stub combining network in [12].

the optimal susceptance control law and amplitude modulation. This mixed-mode control law has three regions of operation as indicated in Fig. 19.

At the highest output power levels, the PA drive power is maximized and output power is controlled using outphasing only (according to the ideal OS control law, equations (14) and (15)). In the region labeled "Outphasing plus drive backoff," a combination of drive amplitude and phase control is used, with the input drive amplitude backed off so that the branch PAs are not over-driven. The drive levels are determined experimentally for highest efficiency while still saturating the branch PAs. At low output power levels, i.e., more than 7 dB below peak output power, the amplitude is modulated alone (with constant outphasing angles). This mixed-mode approach extends the system's output range down to zero.

The peak CW drain efficiency of the system is 72%, with efficiency remaining above 60% over the 7-dB outphasing range. Also shown in Fig. 19 are the CW measurements of a four-way outphasing system using the same PAs but with a four-way radial-stub-based combiner [12]. The two combining networks demonstrate comparable performance and insertion loss, with the slightly compressed efficiency curve in the transmission-line version most likely explained by its "T" layout that introduces asymmetry in the design. The compact layout described in Section III could not be measured experimentally because of the large dimensions of the power amplifiers (simply using cables to connect the PAs and combiner board is complicated by the sensitivity of the system to electrical length between the branch PAs and the combiner reference plane). For a practical, compact, and most efficient version, the power amplifiers and combiner should be integrated on a single PCB.

Fig. 20 shows the CW output power as a function of commanded power P_n (see equations (14)–(15)) when the system is operated in the outphasing and outphasing plus backoff regimes. The nonlinearity near 0 dB commanded power is due to the experimentally determined drive back-off characteristic, which has been chosen for a good efficiency characteristic rather than to optimize linearity. It is clear from this result that some amount of linearization (digital predistortion) would be necessary for this architecture to be used in a modern communications system.
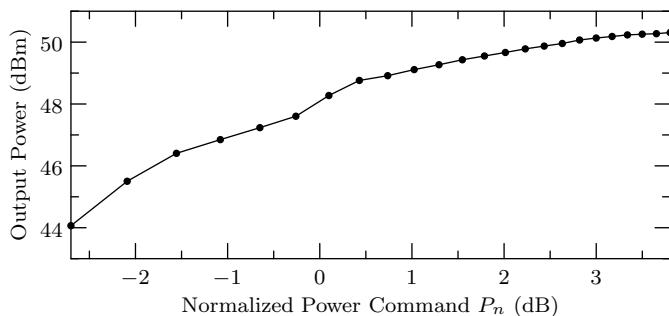
Fig. 20. CW measurement of output power as a function of power command P_n, using control phases determined by the outphasing control law in (14)–(15), in the pure outphasing and outphasing plus back-off regions (see Fig. 19). The $P_n = 0$ dB power point corresponds to a nominal loading impedance on the four PAs of 50 ohms.

C. Modulated Performance

Because the bandwidth and linearity of the baseband signal decomposition setup was limited, this work does not focus on the linearizability of the approach. Nonetheless, the was tested with a 3.84-MHz W-CDMA signal having a 9.15-dB (measured) PAPR, for which the average drain efficiency was 54.5%. Limited digital predistortion (DPD) was applied based on a memoryless LUT and the use of an oscilloscope as an observation receiver. The -34.2 dBc ACLR under these conditions is comparable to the -37.7 dBc ACLR produced from one of the IQ modulators in the signal component separator (the SCS design is described in further detail in [12]). The low ACLR of the experimental setup is a result of the short (repeated) test waveform.

Table I summarizes the performance of this outphasing amplifier in comparison to other state-of-the-art works having similar technology and output power levels. Compared to the authors' previous demonstrations of four-way outphasing techniques, this TL implementation shows comparable efficiency and shares the power-handling capability of the all-microstrip radial stub combiner [12]. The compact TL combiner introduced in this work has an area advantage over the radial combiner, and is expected to scale better (in size and frequency) than previous techniques.

V. CONCLUSION

Outphasing power amplifier systems are attractive solutions to achieve efficiency over a wide dynamic range due to their use of saturated-mode operation. In this work we investigate the operation and design of an outphasing architecture that provides nearly ideal resistive load modulation of branch amplifiers, while enabling use of a microwave-friendly all-transmission-line combining network. The new all-transmission-line multi-way lossless power combining network is effective for compact microwave power amplifier systems.

In order to enable implementation of this idea, we have derived theoretical expressions for branch PA loading conditions and system output power. We present both a design approach and an outphasing control strategy to minimize the variation in susceptive loading impedances for a specified load resistance

TABLE I
COMPARISON TO OTHER WORKS: W-CDMA PERFORMANCE

Ref.	Arch.	Carrier (MHz)	P_{max} (W)	PAPR (dB)	ACLR$_1$ (dBc)	Drain Eff.
[28]	Chireix	2300	70	9.6	-49	53.5%
[50]	Chireix	2140	90	9.6	-47	50.5%
[27]	Chireix	1950	19	9.6	-47	54.5%
[5]	4-way Doherty	2140	100	6.5	-31*	61%
[51]	Saturated Doherty	2140	10	7.4	-28.3*	52.4%
[10]	4-way Discrete	2140	50	3.5	-36.6	57%
[12]	4-way Hybrid	2140	62	9.11	-31.9	50.3%
[12]	4-way Radial	2140	110	9.15	-33.0	55.6%
This Work	4-way TL	2140	105	9.15	-34.2	54.5%

* no predistortion

and output power range. A design example of a compact layout shows that the combining network, operating at a 2.14 GHz carrier frequency, can be fit within a 39.1 mm by 52.8 mm area. Measurements of this network indicate a close match to the theoretical analysis.

The approach is experimentally verified in a 100-W experimental prototype operating at 2.14 GHz, which demonstrates peak CW drain efficiency of 72% and efficiency above 60% over a 7-dB range. When compared directly to the measured results of a related power combining network based on microstrip lines and radial stub elements, the all-transmission-line combining system has nearly the same CW performance. It is anticipated, however, that the transmission-line version of this approach will have better potential to scale to higher-frequency applications due to its tree structure.

APPENDIX A

In Section II we presented a derivation of the input-port admittance characteristics of the four-way combiner of Fig. 1 for a half-wavelength transmission line base length ($\ell_{base} = \lambda/2$). By employing an analogous approach, it can be shown that the four-port admittance matrix Y_{4way} relating the combiner's input port voltages $V_A - V_D$ and currents $I_A - I_D$ for a four-way combiner implemented with a quarter-wavelength base length ($\ell_{base} = \lambda/4$) is given by (20a)-(20e), where $\sigma_1 = 2\pi\Delta_1/\lambda$, $\sigma_2 = 2\pi\Delta_2/\lambda$, $\gamma = R_L/Z_1$, and $\beta = Z_2/Z_1$.

$$\begin{bmatrix} I_A \\ I_B \\ I_C \\ I_D \end{bmatrix} = Y_{eff} \begin{bmatrix} V_A \\ V_B \\ V_C \\ V_D \end{bmatrix} = Y_0 \begin{bmatrix} M_1 & M_2 \\ M_2 & M_3 \end{bmatrix} \begin{bmatrix} V_A \\ V_B \\ V_C \\ V_D \end{bmatrix} \quad (20a)$$

$$M_1 = \begin{bmatrix} \gamma \csc^2 \sigma_2 + j(-\cos\sigma_1 \sin\sigma_1 + \beta\cot\sigma_2) \\ \gamma\csc^2\sigma_2 + j\beta\cot\sigma_2 \end{bmatrix}$$
$$\begin{bmatrix} \gamma\csc^2\sigma_2 + j\beta\cot\sigma_2 \\ \gamma\csc^2\sigma_2 + j(\cos\sigma_1\sin\sigma_1 + \beta\cot\sigma_2) \end{bmatrix} \quad (20b)$$

$$M_2 = \begin{bmatrix} -\gamma\csc^2\sigma_2 & -\gamma\csc^2\sigma_2 \\ -\gamma\csc^2\sigma_2 & -\gamma\csc^2\sigma_2 \end{bmatrix} \quad (20c)$$

$$M_3 = \begin{bmatrix} \gamma\csc^2\sigma_2 - j(\cos\sigma_1\sin\sigma_1 + \beta\cot\sigma_2 \\ \gamma\csc^2\sigma_2 - j\beta\cot\sigma_2 \end{bmatrix}$$
$$\begin{bmatrix} \gamma\csc^2\sigma_2 - j\beta\cot\sigma_2 \\ \gamma\csc^2\sigma_2 - j(-\cos\sigma_1\sin\sigma_1 + \beta\cot\sigma_2) \end{bmatrix} \quad (20d)$$

$$Y_0 = \frac{\sec^2\sigma_1}{Z_1} \quad (20e)$$

Assuming that the PAs are outphased according to the phasor relationship in Fig. 1 with all input-port voltages V_A–V_D having the same magnitude V_S, then one can solve (20) for the effective admittance $Y_{\mathrm{eff},A}$–$Y_{\mathrm{eff},D}$ each of the PAs sees looking into the combiner as a function of the outphasing angles θ and ϕ (21) with all other PAs active. Note that the expressions in (21) are quite similar to the expressions derived for the effective admittances of the four-way combiner with $\ell_{\mathrm{base}} = \lambda/2$ given by (7).

$$Y_{\mathrm{eff},A} = Y_{\mathrm{eff},D}^* = \frac{\csc^2\sigma_2 \sec^2\sigma_1}{Z_1}$$
$$\times [\cos\phi(-\beta\sin\phi\sin(2\sigma_2) + 4\gamma\sin\theta\sin(\theta+\phi))$$
$$+ j\left(-4\gamma\cos\phi\cos(\theta+\phi)\sin\theta\right.$$
$$\left. - \cos\sigma_1\sin\sigma_1\sin^2\sigma_2 + \beta\cos^2\phi\sin(2\sigma_2)\right)] \quad (21a)$$

$$Y_{\mathrm{eff},B} = Y_{\mathrm{eff},C}^* = \frac{\csc^2\sigma_2\sec^2\sigma_1}{Z_1}$$
$$\times [\beta\cos\phi\sin\phi\sin(2\sigma_2) + 4\gamma\sin\theta\cos\phi\sin(\theta-\phi)$$
$$+ j\left(-4\gamma\cos(\theta-\phi)\cos\phi\sin\theta\right.$$
$$\left. + \cos\sigma_1\sin\sigma_1\sin^2\sigma_2 + \beta\cos^2\phi\sin(2\sigma_2)\right)]$$
$$(21b)$$

Furthermore, it can be shown that the output power P_{out} delivered by the four-way combiner to the load in the case of $\ell_{\mathrm{base}} = \lambda/4$ is given by (22), where θ and ϕ are the PA outphasing angles, and V_S is the PA output amplitude according to the phasor diagram in Fig. 1.

$$P_{\mathrm{out}} = \frac{8R_L V_S^2}{Z_1^2 \sin^2\sigma_2 \cos^2\sigma_1} \sin^2\phi\cos^2\theta \quad (22)$$

It can be further shown that the OS control angles θ and ϕ for the case of the four-way combiner with $\ell_{\mathrm{base}} = \lambda/4$ are given by (23) and (24), where $\sigma_1 = 2\pi\Delta_1/\lambda$, $\sigma_2 = 2\pi\Delta_2/\lambda$, and P_{out} is the output power delivered by the combiner to a load R_L.

$$\phi = \mathrm{arccot}\left(\frac{Z_1\cot\sigma_1 P_{\mathrm{out}}}{2V_S^2}\right) \quad (23)$$

$$\theta = \arcsin\left(\sin\sigma_2\sin\sigma_1\sqrt{\frac{4V_S^2 + P_{\mathrm{out}}Z_1^2\cot^2\sigma_1}{8R_L V_S^2 P_{\mathrm{out}}}}\right) \quad (24)$$

APPENDIX B

In this appendix, we further consider the characteristics of the combiner, including its output power control characteristic. Interestingly, one can notice from (12) that the output power P_{out} delivered to the load is independent of the characteristic impedance Z_2 of the output branch transmission lines in the four-way combiner of Fig. 1. To gain insight into this fact, consider again the three-port transmission-line network shown in Fig. 2. Suppose that we short-circuit ports one and two, i.e., $V_1 = 0$ and $V_2 = 0$. Looking into port three, one sees the parallel combination of the two transmission lines connected to ground. Due to the $\pm\Delta$ differential increment in their length, the two transmission lines behave as the parallel combination of a conjugate pair of purely-imaginary impedances to ground (assuming that the transmission lines are lossless), hence resulting in infinite net impedance when looking into port three (with ports one and two short-circuited). Due to the linearity of the three-port network in Fig. 2, we can conclude that the port three input current I_3 is independent of V_3 and is entirely determined by V_1, V_2, and Δ. This is also accordingly reflected by the three-port admittance matrix in (1). This result is valid for any Δ, provided that the base length ℓ_{base} of the transmission lines is an integer multiple of a quarter wavelength, and the transmission lines are treated as lossless. Selecting the transmission line base length ℓ_{base} to be other than an integer multiple of a quarter wavelength results in a non-infinite impedance (at the operating frequency) when looking into port three with ports one and two short-circuited, implying a dependence of I_3 on V_3.

Redirecting our attention to the case of the four-way combiner and applying the above reasoning to Fig. 4 we can now see that the branch currents I_E and I_F are independent of the respective node voltages V_E and V_F and the characteristic impedance Z_2 of the output branch transmission lines. From (8) the load current I_L, and hence output power P_{out}, depends solely on I_E and I_F and the length of the output-branch transmission lines, but not on their characteristic impedance Z_2. It is important to note, however, that although the output power may be independent of Z_2, one must carefully select both transmission-line impedances Z_1 and Z_2 as their values are both of great importance to the overall performance of the combiner and its input-port admittance characteristic (e.g., see Fig. 8).

It is also worth clarifying that selecting Δ_1 to be zero does not result in infinite output power as may be counterintuitively suggested by (12) for the four-way combiner of Fig. 4 with $\ell_{\mathrm{base}} = \lambda/2$. In reality, choosing Δ_1 equal to zero corresponds to a degenerate case of the four-way combiner (see Fig. 4) in which each of the input branch transmission lines is a half-wavelength long. Suppose that all four input ports of the combiner are driven with ideal voltage sources V_A–V_D with zero output impedance according to the phasor diagram in Fig. 1. One can represent each of the input branches (comprising a half-wavelength-long transmission line and ideal voltage source driver) with its Thevenin equivalent having zero Thevenin impedance and a Thevenin voltage that is 180° out of phase with the respective terminal input voltage V_A–V_D.

This effectively results in connecting the PAs that are driving terminals A and B (C and D) in parallel. Practically, this is only possible if terminal pairs A/B and C/D are driven in phase, i.e., $\phi = 0$ in Fig. 1 ($V_A = V_B$ and $V_C = V_D$), or if the output amplitude of all PAs is zero, i.e., $V_S = 0$ in (12). In the former case, the four-way combiner is reduced to a two-way combiner, while in the latter case no power is delivered to the output. As Section II-D describes in detail, selection a smaller value for Δ_1 and Δ_2 results in smaller variation of the combiner's input susceptance over its operating power range. As a tradeoff, however, smaller values for Δ_1 and Δ_2 require transmission line characteristic impedances Z_1 and Z_2 that are relatively high with respect to the combiner's load. The ability to practically implement transmission lines with high characteristic impedances limits how small one can choose Δ_1 and Δ_2.

REFERENCES

[1] L. Kahn, "Single-sideband transmission by envelope elimination and restoration," *Proc. IRE*, vol. 40, no. 7, pp. 803–806, July 1952.

[2] D. Kimball, J. Jeong, C. Hsia, P. Draxler, S. Lanfranco, W. Nagy, K. Linthicum, L. Larson, and P. Asbeck, "High-efficiency envelope-tracking W-CDMA base-station amplifier using GaN HFETs," *IEEE Trans. Microw. Theory Techn.*, vol. 54, no. 11, pp. 3848–3856, 2006.

[3] H. Tango, T. Hashinaga, K. Totani, H. Kuriyama, Y. Hamada, and T. Asaina, "A 60% efficient envelope tracking power amplifier for 40W, 2.6GHz LTE base station with in/output harmonic tuning," in *IEEE MTT-S Int. Micro. Symp. Dig.*, June 2013, pp. 1–4.

[4] M. Pelk, W. Neo, J. Gajadharsing, R. Pengelly, and L. de Vreede, "A high-efficiency 100-W GaN three-way doherty amplifier for base-station applications," *IEEE Trans. Microw. Theory Techn.*, vol. 56, no. 7, pp. 1582–1591, 2008.

[5] A. Grebennikov, "A high-efficiency 100-W four-stage Doherty GaN HEMT power amplifier module for WCDMA systems," in *IEEE MTT-S Int. Microw. Symp. Dig.*, June 2011, pp. 1–4.

[6] H. Deguchi, N. Watanabe, A. Kawano, N. Yoshimura, N. Ui, and K. Ebihara, "A 2.6GHz band 537W peak power GaN HEMT asymmetric Doherty amplifier with 48% drain efficiency at 7dB," in *IEEE MTT-S Int. Microw. Symp. Dig.*, June 2012, pp. 1–3.

[7] H. Chireix, "High power outphasing modulation," *Proceedings of the IRE*, vol. 23, no. 11, pp. 1370–1392, Nov. 1935.

[8] D. Perreault, "A new power combining and outphasing modulation system for high-efficiency power amplification," *IEEE Trans. Circuits Syst. I: Reg. Papers*, vol. 58, no. 8, pp. 1713–1726, Feb. 2011.

[9] A. Jurkov, L. Roslaniec, and D. Perreault, "Lossless multi-way power combining and outphasing for high-frequency resonant inverters," *IEEE Trans. Power Electron.*, vol. 29, no. 4, pp. 1894–1908, April 2014.

[10] T. W. Barton, J. L. Dawson, and D. J. Perreault, "Experimental validation of a four-way outphasing combiner for microwave power amplification," *IEEE Microw. Wireless Compon. Lett.*, vol. 23, no. 1, pp. 28–30, Jan. 2013.

[11] T. W. Barton, J. L. Dawson, and D. J. Perreault, "Four-way lossless outphasing and power combining with hybrid microstrip/discrete combiner for microwave power amplification," in *IEEE MTT-S Int. Microw. Symp. Dig.*, June 2013, pp. 1–4.

[12] T. Barton and D. Perreault, "Four-way microstrip-based power combining for microwave outphasing power amplifiers," *IEEE Trans. Circuits and Systems I: Regular Papers*, vol. 61, no. 10, pp. 2987–2998, Oct 2014.

[13] A. Jurkov and D. Perreault, "Design and control of lossless multi-way power combining and outphasing systems," in *Midwest Symp. Circuits Syst.*, Aug. 2011, pp. 1–4.

[14] A. Jurkov, L. Roslaniec, and D. Perreault, "Lossless multi-way power combining and outphasing for high-frequency resonant inverters," pp. 910–917, June 2012.

[15] T.-P. Hung, D. Choi, L. Larson, and P. Asbeck, "CMOS outphasing class-D amplifier with Chireix combiner," *IEEE Microw. Wireless Compon. Lett.*, vol. 17, no. 8, pp. 619–621, 2007.

[16] S. Lee and S. Nam, "A CMOS outphasing power amplifier with integrated single-ended Chireix combiner," *IEEE Trans. Circuits Syst. II: Exp. Briefs*, vol. 57, no. 6, pp. 411–415, 2010.

[17] F. Raab, "Efficiency of outphasing RF power-amplifier systems," *IEEE Trans. Commun.*, vol. 33, no. 10, pp. 1094–1099, Oct. 1985.

[18] A. Birafane and A. Kouki, "On the linearity and efficiency of outphasing microwave amplifiers," *IEEE Trans. Microw. Theory Techn.*, vol. 52, no. 7, pp. 1702–1708, July 2004.

[19] F. Raab, P. Asbeck, S. Cripps, P. Kenington, Z. Popovic, N. Pothecary, J. Sevic, and N. Sokal, "Power amplifiers and transmitters for RF and microwave," *IEEE Trans. Microw. Theory Techn.*, vol. 50, no. 3, pp. 814 –826, Mar. 2002.

[20] I. Hakala, D. Choi, L. Gharavi, N. Kajakine, J. Koskela, and R. Kaunisto, "A 2.14-GHz Chireix outphasing transmitter," *IEEE Trans. Microw. Theory Techn.*, vol. 53, no. 6, pp. 2129–2138, June 2005.

[21] N. Singhal, H. Zhang, and S. Pamarti, "A zero-voltage-switching contour-based outphasing power amplifier," *IEEE Trans. Microw. Theory Techn.*, vol. 60, no. 6, pp. 1896–1906, June 2012.

[22] M. El-Asmar, A. Birafane, M. Helaoui, A. Kouki, and F. Ghannouchi, "Analytical design methodology of outphasing amplification systems using a new simplified Chireix combiner model," *IEEE Trans. Microw. Theory Techn.*, vol. 60, no. 6, pp. 1886–1895, 2012.

[23] P. Landin, J. Fritzin, W. Van Moer, M. Isaksson, and A. Alvandpour, "Modeling and digital predistortion of class-D outphasing RF power amplifiers," *IEEE Trans. Microw. Theory Tech*, vol. 60, no. 6, pp. 1907–1915, 2012.

[24] T. Ni and F. Liu, "A new impedance match method in serial Chireix combiner," in *Asia-Pacific Microw. Conf.*, 2008, pp. 1–4.

[25] W. Gerhard and R. Knoechel, "Improved design of outphasing power amplifier combiners," in *German Microw. Conf.*, 2009, pp. 1–4.

[26] R. Beltran, F. Raab, and A. Velazquez, "HF outphasing transmitter using class-E power amplifiers," in *IEEE MTT-S Int. Microw. Symp. Dig.*, June 2009, pp. 757–760.

[27] M. van der Heijden, M. Acar, J. Vromans, and D. Calvillo-Cortes, "A 19W high-efficiency wide-band CMOS-GaN class-E Chireix RF outphasing power amplifier," in *IEEE MTT-S Int. Microw. Symp. Dig.*, June 2011, pp. 1–4.

[28] D. Calvillo-Cortes, M. van der Heijden, and L. de Vreede, "A 70W package-integrated class-E Chireix outphasing RF power amplifier," in *IEEE MTT-S Int. Microw. Symp. Dig.*, June 2013, pp. 1–3.

[29] T. Barton and D. Perreault, "An RF-input outphasing power amplifier with RF signal decomposition network," in *IEEE Int. Microw. Symp*, May 2015, pp. 1–4.

[30] ——, "Theory and implementation of RF-input outphasing power amplification," *IEEE Trans. Microw. Theory Techn.*, vol. 63, no. 12, pp. 4273–4283, Dec 2015.

[31] N. Faraji and T. Barton, "An RF-input Chireix outphasing power amplifier," in *IEEE Radio and Wireless Symposium*, January 2016, pp. 1–3.

[32] J. Yao and S. Long, "Power amplifier selection for LINC applications," *IEEE Trans. Circuits Syst. II: Exp. Briefs*, vol. 53, no. 8, pp. 763–767, Aug. 2006.

[33] F. Raab, P. Asbeck, S. Cripps, P. Kenington, Z. Popovic, N. Pothecary, J. Sevic, and N. Sokal, "RF and microwave power amplifier and transmitter technologies – part 3," *High Frequency Electronics*, pp. 34–48, Sept. 2003.

[34] R. Langridge, T. Thornton, P. Asbeck, and L. Larson, "A power re-use technique for improved efficiency of outphasing microwave power amplifiers," *IEEE Trans. Microw. Theory Techn.*, vol. 47, no. 8, pp. 1467–1470, Aug. 1999.

[35] X. Zhang, L. Larson, P. Asbeck, and R. Langridge, "Analysis of power recycling techniques for RF and microwave outphasing power amplifiers," *IEEE Trans. Circuits Syst. II: Analog Digit. Signal Process.*, vol. 49, no. 5, pp. 312–320, 2002.

[36] P. Godoy, D. Perreault, and J. Dawson, "Outphasing energy recovery amplifier with resistance compression for improved efficiency," *IEEE Trans. Microw. Theory Techn.*, vol. 57, no. 12, pp. 2895–2906, 2009.

[37] D. Cox, "Linear amplification with nonlinear components," *IEEE Trans. Commun.*, vol. COM-23, pp. 1942–1945, Dec. 1974.

[38] T. Barton, "Not just a phase: Outphasing power amplifiers," *IEEE Microw. Magazine*, vol. 17, no. 2, pp. 18–31, Feb 2016.

[39] F. Raab, "High-efficiency linear amplification by dynamic load modulation," in *IEEE MTT-S Int. Microw. Symp. Dig.*, June 2003, pp. 1717–1720.

[40] ——, "Electronically tuned power amplifier," US Patent 7,202,734, April 2007.

[41] H. Nemati, C. Fager, U. Gustavsson, R. Jos, and H. Zirath, "Design of varactor-based tunable matching networks for dynamic load modulation of high power amplifiers," *IEEE Trans. Microw. Theory Techn.*, vol. 57, no. 5, pp. 1110–1118, 2009.

[42] Y. Chen, K. Jheng, A. Wu, H. Tsao, and B. Tzeng, "Multilevel LINC system design for wireless transmitters," in *International Symposium on VLSI Design, Automation and Test*, 25-27 2007, pp. 1–4.

[43] P. A. Godoy, S. Chung, T. W. Barton, D. J. Perreault, and J. L. Dawson, "A 2.4-GHz, 27-dBm asymmetric multilevel outphasing power amplifier in 65-nm CMOS," *IEEE J. Solid-State Circuits*, vol. 47, no. 10, pp. 2372–2384, Oct. 2012.

[44] W. Gerhard and R. Knoechel, "Novel transmission line combiner for highly efficient outphasing RF power amplifiers," in *European Microwave Conference*, 2007, pp. 1433–1436.

[45] R. Beltran and F. Raab, "Simplified analysis and design of outphasing transmitters using class-E power amplifiers," in *IEEE Topical Meeting on Power Amplifiers for Wireless and Radio Applications*, January 2015, pp. 16–18.

[46] T. W. Barton, A. S. Jurkov, and D. J. Perreault, "Transmission-line-based multi-way lossless power combining and outphasing system," in *IEEE MTT-S International Microwave Symposium*, June 2014, pp. 1–4.

[47] L. Roslaniec, A. Jurkov, A. Al Bastami, and D. Perreault, "Design of single-switch inverters for variable resistance / load modulation operation," *IEEE Trans. Power Elec.*, vol. 30, no. 6, pp. 3200–3214, June 2015.

[48] M. Borage, M. V. Nagesh, M. S. Bhatia, and S. Tiwari, "Resonant immittance converter topologies," *IEEE Trans. Ind. Elec.*, vol. 58, no. 3, pp. 971–978, 2011.

[49] G. Kompa, *Practical Microstrip Design and Applications*. Norwood, MA: Artech House, 2005.

Taylor W. Barton (S'07, M'12) received the Sc. B., M.Eng., E.E., and Sc.D degrees from the Massachusetts Institute of Technology, Cambridge, MA. In 2014 she joined The University of Texas at Dallas, where she is currently an Assistant Professor. Prior to joining UT Dallas, she was a Postdoctoral Associate in the MIT Microsystems Technology Laboratories. Her research interests include high-efficiency RF, power, analog circuit design, and classical control theory.

Alexander S. Jurkov (S07) received the B.S. degree in electrical engineering and computer science from the University of Calgary, Calgary, AB, Canada in 2010, and the S.M. degree in electrical engineering from the Massachusetts Institute of Technology (MIT), Cambridge, in 2012. He is currently pursuing his Ph.D. degree in the area of power electronics and radio-frequency system design at the Laboratory of Electronic and Electromagnetic Systems at MIT.

In 2012, he worked for Analog Devices Inc., Woburn, MA on the design of integrated high-speed data buffers and their realization with a 24nm technology. His research interests include RF power converters, amplifiers, combiners, and mixed-signal and embedded system design.

Prathamesh H. Pednekar (S15) received the B.E. degree in electronics and telecommunication from University of Mumbai, India in 2012. He is currently working toward the M.S. degree from University of Texas at Dallas, Texas. Prior to joining UT Dallas in 2014, he worked as a Research Scientist at Society for Applied Microwave Electronic Engineering and Research, Mumbai.

His research interests include RF Power Amplifiers design, Passive Microwave components and Phased array radar.
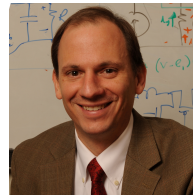
David J. Perreault (S'91, M'97, SM'06, F'13) received the B.S. degree from Boston University, Boston, MA, and the S.M. and Ph.D. degrees from the Massachusetts Institute of Technology, Cambridge, MA. In 1997 he joined the MIT Laboratory for Electromagnetic and Electronic Systems as a Postdoctoral Associate, and became a Research Scientist in the laboratory in 1999. In 2001, he joined the MIT Department of Electrical Engineering and Computer Science, where he is presently Professor and Associate Department Head. His research interests include design, manufacturing, and control techniques for power electronic systems and components, and in their use in a wide range of applications. He also consults in industry, and is co-founder of Eta Devices, a startup company focusing on high-efficiency RF power amplifiers. Dr. Perreault received the Richard M. Bass Outstanding Young Power Electronics Engineer Award, the R. David Middlebrook Achievement Award, the ONR Young Investigator Award, and the SAE Ralph R. Teetor Educational Award, and is co-author of seven IEEE prize papers.